Supplementary Materials

Parameter-free resolution estimation based on decorrelation analysis

1. Mathematical framework- *derivation of the analytical expression of the decorrelation function d(r)*

We consider an incoherent imaging apparatus characterized by the ideal transfer function $H(k)$ of frequency support k_{th}:

$$H(k) = \begin{cases} 1 - \dfrac{|k|}{k_{th}} & |k| < k_{th} \\ 0 & otherwise \end{cases} \tag{S1}$$

where $k = \sqrt{k_x^2 + k_y^2}$. We image an idealized point emitter of brightness A located on the optical axis. During the acquisition, the image is corrupted with pure white noise. The resulting intensity $I(k)$ is expressed in Fourier space, as

$$I(k) = A\left(1 - \frac{|k|}{k_{th}}\right)(|k| < k_{th}) + e^{i\theta(k)} \tag{S2}$$

where $\theta(k)$ is the random phase of the white noise.

The decorrelation analysis, i.e. the computation of the partial phase cross-correlation between the original image and its normalized version is expressed in Fourier space as

$$d(r) = \frac{\iint_{-\infty}^{\infty} Re\left\{I(k)\frac{I^*(k)}{|I(k)|}M(k;r)\right\}dk_x dk_y}{\sqrt{\iint_{-\infty}^{\infty}|I(k)|^2 dk_x dk_y \iint_{-\infty}^{\infty}\left|\frac{I(k)}{|I(k)|}M(k;r)\right|^2 dk_x dk_y}} \tag{S3}$$

where $M(k;r)$ is a binary mask of radius r. The expression of the partial phase correlation in Fourier space allows us to make several general considerations. Using complex arithmetic, the numerator can be simplified as $I(k)\frac{I^*(k)}{|I(k)|} = |I(k)|$, while the denominator is composed of two terms. The first is simply the energy of the input image. This number does not depend on r and normalizes the function $d(r)$ between 0 and 1. Finally, due to the normalization, the last term is equal to the mask $\left|\frac{I(k)}{|I(k)|}M(k;r)\right|^2 = M(k;r)$.

Transforming equation S3 to polar coordinates $[k_x, k_y] => [k_r, \theta]$, we obtain

$$d(r) = \frac{\int_0^{2\pi}\int_0^1 |I(k)|M(k;r)k_r dk_r d\theta}{\sqrt{E\int_0^{2\pi}\int_0^1 M(k;r)k_r dk_r d\theta}} \tag{S4}$$

where E stands for the energy of the input image (which is independent over coordinate transform) and where we used the Cartesian-Polar transformation $dk_x dk_y = k_r dk_r d\theta$.

Using the simplified imaging model introduced above, it is possible to analytically solve the expression for $d(r)$ and get a better understanding of how the function depends on the image transfer function.

We start with the numerator of equation S4 and use the fact that the mask $M(k;r)$ is 0 for $k_r > r$.

$$\int_0^{2\pi}\int_0^1 |I(k)|M(k;r)k_r dk_r 2d\theta = 2\pi \int_0^r \left| A\left(1-\frac{|k|}{k_{th}}\right)(|k|<k_{th}) + e^{i\theta(k)} \right| k_r dk_r \tag{S5}$$

In order to be able to integrate the noise term $e^{i\theta(k)}$ analytically, we make the additional assumption that the random phase fluctuations averages out under integration, which allows to approximate the expression S5 as the sum of the transfer function and the noise:

$$\begin{aligned} 2\pi \int_0^r \left| A\left(1-\frac{|k|}{k_{th}}\right)(|k|<k_{th}) + e^{i\theta(k)} \right| k_r dk_r \\ \approx 2\pi \int_0^r A\left(1-\frac{|k|}{k_{th}}\right)(|k|<k_{th}) k_r dk_r + \pi r^2 \end{aligned} \tag{S6}$$

The remaining integration is trivial and we obtain for the numerator of equation S4

$$d_{num}(r) \approx \begin{cases} 2\pi A\left(\frac{r^2}{2}-\frac{r^3}{3k_{th}}\right) + \pi r^2 & for\ r \le k_{th} \\ \frac{\pi A}{3}k_{th}^2 + \pi r^2 & for\ r > k_{th} \end{cases} \tag{S7}$$

Using similar argumentation, we can express the signal energy E as

$$E = \pi\left[\frac{A^2 k_{th}^2}{6} + \frac{2Ak_{th}^2}{3} + 1\right] \tag{S8}$$

and the normalized denominator term of equation S4 as

$$\int_0^{2\pi}\int_0^1 M(k;r)k_r dk_r d\theta = \pi r^2 \tag{S9}$$

Using equations S7, S8 and S9, we obtain for the decorrelation function $d(r)$ (for $r < k_{th}$)

$$d(r) = \frac{2\pi A\left(\frac{r^2}{2}-\frac{r^3}{3k_{th}}\right) + \pi r^2}{\sqrt{\pi\left[\frac{A^2 k_{th}^2}{6} + \frac{2Ak_{th}^2}{3} + 1\right]\pi r^2}} \tag{S10}$$

From S10, we clearly see that if $A \ll 1$, i.e. the signal is extremely weak compared to the noise , the decorrelation function becomes a line with a slope of 1.

$$d_{A\ll 1}(r) \approx \frac{\pi r^2}{\sqrt{\pi^2 r^2}} = r \tag{S11}$$

We find the position of the local maxima by computing the partial derivative of the analytical expression of equation S10 with respect to r. We find

$$r_{max} = \frac{3k_{th}(A+1)}{4A} \tag{S12}$$

We would like to note that the expression S12 is only valid for $r < k_{th}$ and that $r_{max} = k_{th}$ when $A = 3$. For this basic model, an amplitude below 3 will not yield any local maxima.

This result shows that, as long as the signal is strong enough, there is always a local maximum. Moreover, the position of the local maximum is directly connected to the cutoff frequency k_{th}.

Following our mathematical framework, in Figure S1a , we calculate decorrelation function $d(r)$ with (orange, corresponds to equation S10) and without (blue) idealized noise as well as their corresponding transfer functions (orange and blue dashed lines). The position of the local maxima of the orange curve corresponds exactly to the analytical expression. We observe a deviation from the theoretical model when dealing with white noise. The fact that the maximum shifts to a lower frequency (and that its amplitude decreases) translates the degradation of the transfer function (the cutoff frequency is no more clearly identifiable).

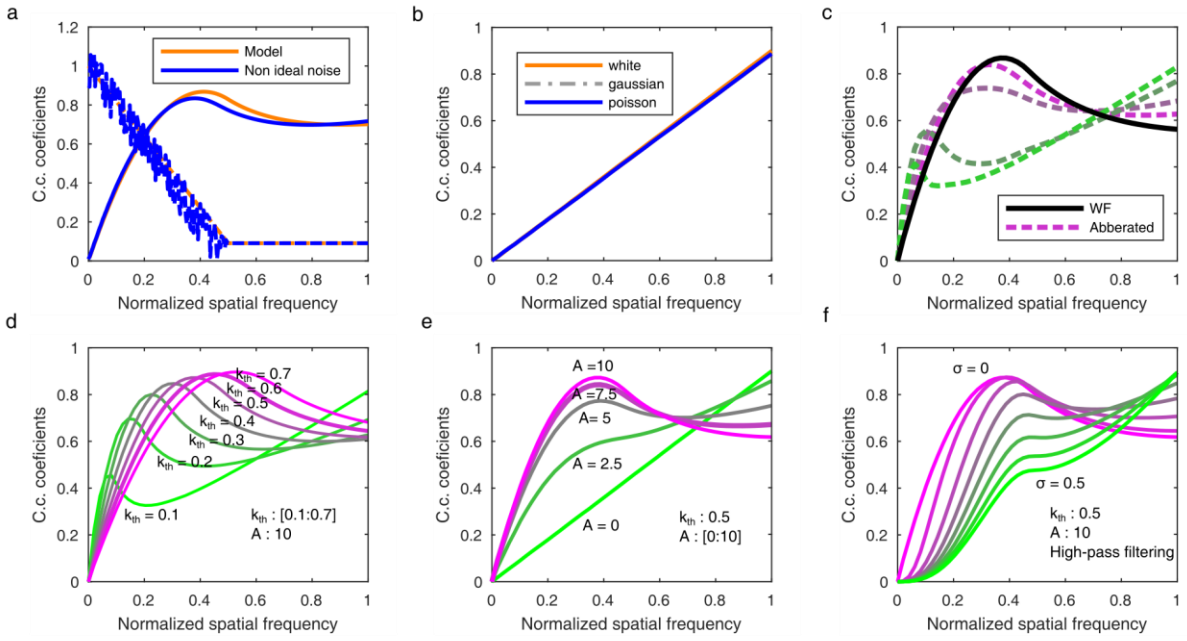

Figure S1: Detailed behavior of decorrelation analysis. (a) Comparison of idealized vs non-ideal noise for the function $d(r)$ (solid lines) and radial average of the Transfer function (dashed line). (b)The plot of d(r) for three different noise statistics. (c) The plot of d(r) for aberration-free and aberrated point-spread function. (d) The plot of d(r) for fixed amplitude and varying cutoff. (e) The plot of d(r) for fixed cutoff and varying amplitude. (f)The plot of d(r) for various high-pass filtering of the input image.

We also show in Figure S1b computation of $d(r)$ for various noise figures (white noise, Gaussian and Poisson). Here, we observe a very interesting feature of the algorithm. Spatially uncorrelated signal corresponds to a straight line, independently of the noise statistics. The fact that the functions are not equal to 1 for $r = 1$ is due to the fact that their power spectral densities are not perfectly flat.

We also illustrate in Figure S1c, d and e, how $d(r)$ evolves as a function of aberrations, the cutoff frequency and the Signal-to-Noise ratio. For aberrations, we computed multiple transfer functions with a fixed cutoff $(k_{th} = 0.5)$ and SNR $(A = 10)$ and increased defocus by adding a circular symmetric quadratic phase $\left(e^{iWr^2}\right)$ to the pupil function, with W varying between 0 and 100. As expected, increases in defocus shifts the position of the maxima to the left. The decrease in the amplitude of the maximum is due to a decrease in SNR due to the spread of the point-spread function. A similar effect is seen when varying the cutoff frequency (Fig. S1d) from 0.7 to 0.1, where the position of the maximum follows the cutoff frequency. Again, the change in amplitude is due to the fact that the total energy of the signal decreases with the cutoff while the noise energy remains constant. On the contrary, when keeping the cutoff frequency fixed and changing the SNR via the parameter A, we observe that the position of the peak does not change until the signal is too weak to produce a peak. This corresponds to the limit of the method.

Finally, we show how $d(r)$ behave when the input image is filtered with a high-pass filter (in our case, we use a standard inverted Gaussian). As we increase the filtering strength, the position of the maximum shifts towards higher-frequencies. At some point we observe that too much signal has been removed from the image as no more peaks are observable. By filtering the input image, we are effectively modifying the transfer function in order to emphasize the high-frequencies. This provides a unique and robust way of estimating the resolution of the image based on the position of the peaks.

We also notice that our analysis intrinsically produces smooth and noiseless functions, without the need to apply any additional smoothing or any kind of fit. This is due to the fact that the function is computed by integration over a disk of radius r. Two neighboring values $d(r)$ and $d(r + \Delta r)$ share a large amount of information. They are therefore naturally correlated and evolve slowly with respect to r.

1.1. Resolution criterion, frequency sampling and error estimation

So far, we have introduced a way to process an image to extract several curves that exhibit a local maximum directly linked to the spatial frequency content of the image. The remaining operation consists of selecting the most suitable peak to be our resolution estimator. We consider the two most natural choices that are: the peak corresponding to the highest frequency $\left(k_{c,m} = \max_{i=[1,N_g]} r_i\right)$ or the peak corresponding to the highest geometrical mean $\left(k_{c,GM} = r_i \mid \max_{i=[1,N_g]} \sqrt{r_i A_i}\right)$ (giving the same amount of weight to the amplitude of the peak, i.e. SNR, and the spatial frequency).

We conducted a large study, computing the resolution using both criteria, with a varying sampling of $d(r)$ (N_r= [30:100] in steps of 10) and different numbers of high-pass filtering (N_g= [10:30] in steps of 5). Figure S2a displays the STED image used to show how the resolution estimated from the highest frequency $\left(k_{c,m}\right)$ changes with respect to Nr and Ng.

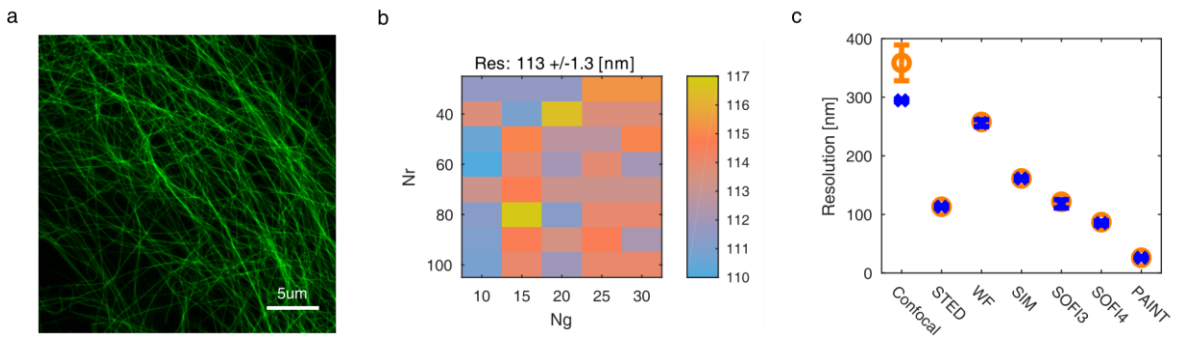

Figure S2: Resolution estimate and criterion vs N_r and N_g. (a) STED image used as an example for (b). (b) Estimated resolution of (a) as a function of N_r and N_g, with an average and standard deviation of 113±1.3nm . (c) Resolution estimate average and standard deviation for different modalities and the two resolution criteria: geometric mean (orange circles) and highest frequency (blue crosses). (Confocal: Fig. 2a, STED: Fig. 2c, WF: Fig. 3a, SIM: Fig. 3c, SOFI3-4: Fig. 4a and PAINT: Fig. 5f).

Figure S2b shows the resolution estimate using the maximum frequency criterion $res = 2/k_{c,m}$, where $k_{c,m}$ is expressed in [1/um] as a function of N_r and N_r. Using the geometric mean criterion, we measure an average resolution of $113nm$ and a precision of $\pm$ $1.8nm$ (not shown here) and $113 \pm 1.3nm$ using the maximum frequency (see Fig. S2b). This demonstrates the robustness of the method to large changes in processing parameters and the absence of bias introduced by the choice of the parameters. Figure S2c shows the same comparison for different imaging modalities presented in the main text (Fig. 2-5). Besides for confocal data, there is no significant difference between the estimated resolution using the geometric mean (orange circles) or the maximum frequency (blue crosses) criteria and the precision is typically $\pm 3nm$ or less. The reason why the confocal data has a different behavior is linked to the shape of its transfer function and can be directly seen in Figure 2. The amplitude of the peaks drops very quickly for a small increase in spatial frequency. This is due to the fact that confocal transfer function has a quadratic decrease in amplitude as a function of spatial frequency. Therefore, the criterion that includes SNR is more likely to be conservative when estimating the resolution.

Unlike specified otherwise, all resolutions and cutoff frequencies shown in the manuscript are calculated using the highest frequency criterion.

1.2. Algorithm implementation

The following section describes the implementation of the method. The source code is publicly available on github (https://github.com/Ades91/ImDecorr.git) and is currently implemented in Matlab (CPU and GPU) and Java (CPU, as an ImageJ plugin, see Section 8).

I. Pre-processing

We first compute the mean and subtract it from the image. We then apodize the edges by multiplying the image with a cosine window function defined as

$$W(x) = \begin{cases} \cos(k_x|x| + \varphi) & |x| \geq x_{max} - w \\ 1 & |x| < x_{max} - w \end{cases} \quad \text{(S13)}$$

where $x \in [-x_{max}, x_{max}]$, x_{max} is half the field of view, w is the window length, $k_x = \frac{\pi}{w}$ and $\varphi = \pi - \frac{\pi}{w} x_{max}$. High frequency artefacts arising for edge discontinuities are consequently minimized. The image is then Fourier transformed and all values for $r > 1$, where r is the normalized radial frequency, are set to 0.

II. Initial decorrelation computation and peak finding

The initial decorrelation function $d(r)$ is computed according to equation (1) from main text. For speed consideration, the computation is performed in Fourier space as

$$d(r) = \frac{\sum\sum_{k_x,k_y} Re\{I(k_x,k_y) M(r) I_n(k_x,k_y)^*\}}{\sqrt{\sum\sum_{k_x,k_y} |M(r) I_n(k_x,k_y)|^2 \sum\sum_{k_x,k_y} |I(k_x,k_y)|^2}} \quad \text{(S14)}$$

As discussed in the theoretical framework (see Section 1), the function $d(r)$ has a local maximum which we need to locate. This is a very general signal processing task and many solutions exist. In our case, the decorrelation function always exhibit a highly specific shape where it is equal to 0 for $r = 0$, raises to a certain value based on the SNR and decreases as it decorrelates. Using our knowledge of the shape of $d(r)$, we propose the following strategy for determining the local maxima.

We pick the maximum of $d(r)$. If the position of the picked maximum is the last value of the array, this means that either the tail of $d(r)$ is larger than the local maximum or there is no local maximum. In both cases, we exclude the value from the array and repeat the operation with the remaining values. We stop the loop as soon as we find a maximum that is not the last element of the array (local maximum exists) or if we run out of values (no local maxima at all). By processing a significant amount of simulated and experimental images, we concluded that our strategy for localizing the local maximum of any decorrelation function was robust enough and that we did not need to implement more sophisticated approach.

In order to avoid the selection of noisy local maxima (very rarely arising when analyzing post-processed or poorly sampled images), we also impose that the local maximum should be at least 0.001 larger than the smallest value from the position of the maximum to the last value of the array. We point out the fact that, unlike the Fourier Ring Correlation or Power Spectral Density threshold, it cannot be used to tune the resolution as it works only as a **rejection criterion** and is only useful in very specific situations rather than being mandatory.

The average image SNR estimate is set as $A_0 = d(r_0)$ and the position of the local maximum of r_0 is used as a first guess for the spatial frequency content, useful for the following high-pass refinement steps (Fig. 1c).

III. High-pass filtering and resolution estimation

In order to find the highest significant frequency, the input image has to be high-pass filtered in a smooth way, in order to weaken low frequencies contributions. Here we propose the use of Gaussian filtering. In both Matlab and ImageJ implementation, this operation is performed in real space (conveniently using B = imgaussfilt(A) for Matlab or the GaussianBlur() class for

ImageJ). This operation could also be implemented in Fourier space for processing speed optimization. We obtain the high-pass filtered version of the image I as:

$$I_{HP}(x) = I(x) - I_{LP}(x;\sigma) \tag{S15}$$

where $I_{LP}(x;\sigma)$ is the low-pass version of the image with a σ.

In the current implementation, we propose to compute N_g (typically 10) high-pass version of the input image with $\sigma_i = e^{\frac{i}{N_g}\left(\log\left(\frac{2}{r_0}\right)-\log(0.15)\right)+\log(0.15)}$. Each σ is then exponentially distributed between $\frac{2}{r0}$ (weak high-pass) and 0.15 (very strong high-pass) where r_0 is expressed in pixels units. For each high-pass filtered image, a corresponding decorrelation function is computed and the local maximum position and amplitude are extracted $[r_i, A_i]$.

We then get the highest frequency peak and the largest geometric mean from all peaks.

The σ_B corresponding to the "best" curve is identified for both criterion and the whole procedure is repeated with refined high-pass filtering distributed between $\min(\sigma_{B,gm}, \sigma_{B,max})$ and $\max(\sigma_{B+1,gm}, \sigma_{B+1,max})$.

While it is not the fastest implementation (more advanced method could be used to improve the convergence and minimize the number of correlations to be computed), it guarantees a result in a fixed and reasonable computation time (typical processing speeds are ranging from 1 to 15 seconds depending on the implementation, the size of the image and the number of points N_r and N_g used for the computation).

The image resolution is then defined as $resolution = \frac{2}{k_c}$, where $k_c = \max_{i=[1,N_g]} r_i$ is expressed in [1/um].

2. *Simulations*

2.1. Point emitters

To validate the ability of the proposed analysis in estimating the resolution and Signal-to-Noise Ratio (SNR), we performed additional simulations. The simulated object consists in a random distribution of point emitters, contributing incoherently to the image intensity. The image SNR is controlled by the amplitude of the incoherent point spread function and the resolution is controlled by the extent of the transfer function $H(k)$. We then compute several images with a cutoff frequency ranging from 0 to 0.8. The incoherent transfer function $H(k)$ can be expressed as

$$H(k) = \begin{cases} A\left(1 - \frac{|k|}{k_{th}}\right) & |k| < k_{th} \\ 0 & otherwise \end{cases} \tag{S16}$$

where k_{th} is the theoretical cutoff frequency and A controls the amplitude of the transfer function. The noise level is controlled by Gaussian additive noise of statistic 100+/-2 counts (corresponding to averaged dark frames statistics of a Hamamatsu Orca Flash V4.0) and additional Poisson noise.

Consequently, we can attribute to each simulated image a theoretical resolution k_{th} and a signal to noise ratio $SNR = \frac{\mu_{sig}}{\sigma_{noise}} = \frac{<I(x)>-100}{2}$. We then vary the image resolution over the range $k_{th} = [0,0.8]$ and the image SNR over $SNR = [0,500]$ (via adequate tuning of A).

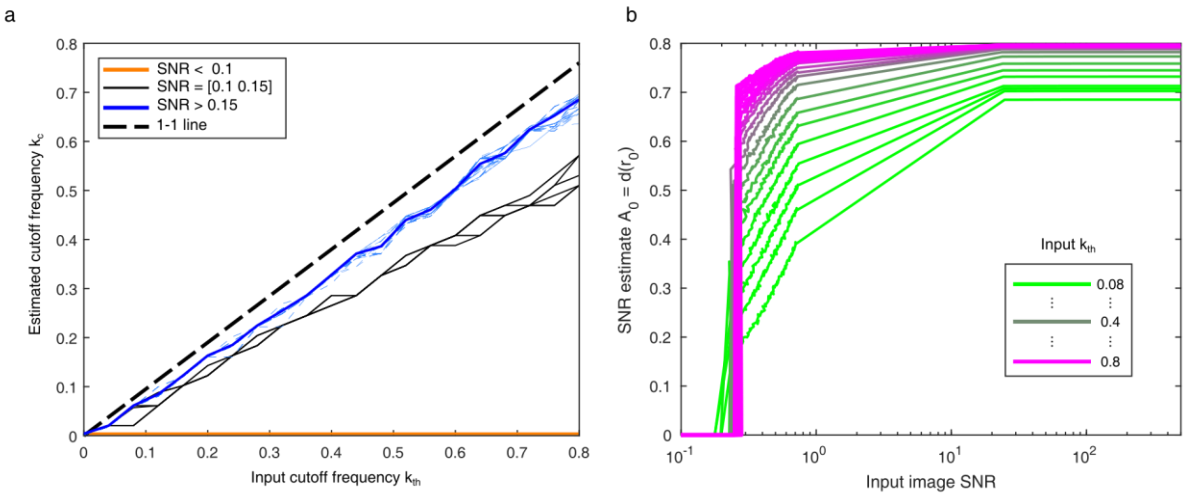

Figure S3: Simulations (a) Estimated cutoff frequency vs simulated NA for various image SNR (Orange line: SNR < 0.1, Solid black lines: SNR between [0.1 and 0.15], Solid blue line: SNR > 0.15 (average of dashed blue lines), Dashed black line: 1-1 reference line). (b) The amplitude of the initial decorrelation function vs simulated image SNR for various normalized cutoff frequency

Our algorithm exhibits (Fig. S3a) a linear dependency with the simulated cutoff k_{th}, with an offset of about 10% when the image SNR is above ≈ 0.15. $H(k)$ drops to 0 at the frequency k_{th}. In the case of lower SNR, this frequency cannot be reliably estimated. For an image SNR between 0.1 and 0.15, the algorithm recovers a lower resolution, which is consistent when considering low SNR images where the transfer function is partially embedded in the noise. Images with a SNR smaller than 0.1 do not exhibit any peaks in the analysis.

Fig. S3b shows the amplitude A_0 of the peak of the original decorrelation function without any high-pass filtering. While the cutoff frequency estimate is independent of the image SNR (in the high SNR case), we see that our SNR estimator depends on both the input image SNR and the cutoff frequency. This is due to the fact that, in our simulation, we are keeping the amplitude of the transfer function $H(k)$ constant as a function of the cutoff frequency k_{th}. This means that the signal energy (that is the volume under the surface defined by $H(k)$) decreases with the cutoff. Since we are keeping the noise energy constant, the SNR decreases with reduced cutoff, which is what we observe. A detailed plot of the functions is shown in Fig. S1d.

2.2. The modulation transfer function (MTF)

One of the important tools by which image resolution is measured is the Modulation Transfer Function (MTF). This object consists of a series of parallel lines with progressively decreased spacing (Fig. S4a-c). As the lines get closer, the line modulation contrast $\left(M = \frac{I_{max}-I_{min}}{I_{max}+I_{min}}\right)$ drops to 0.

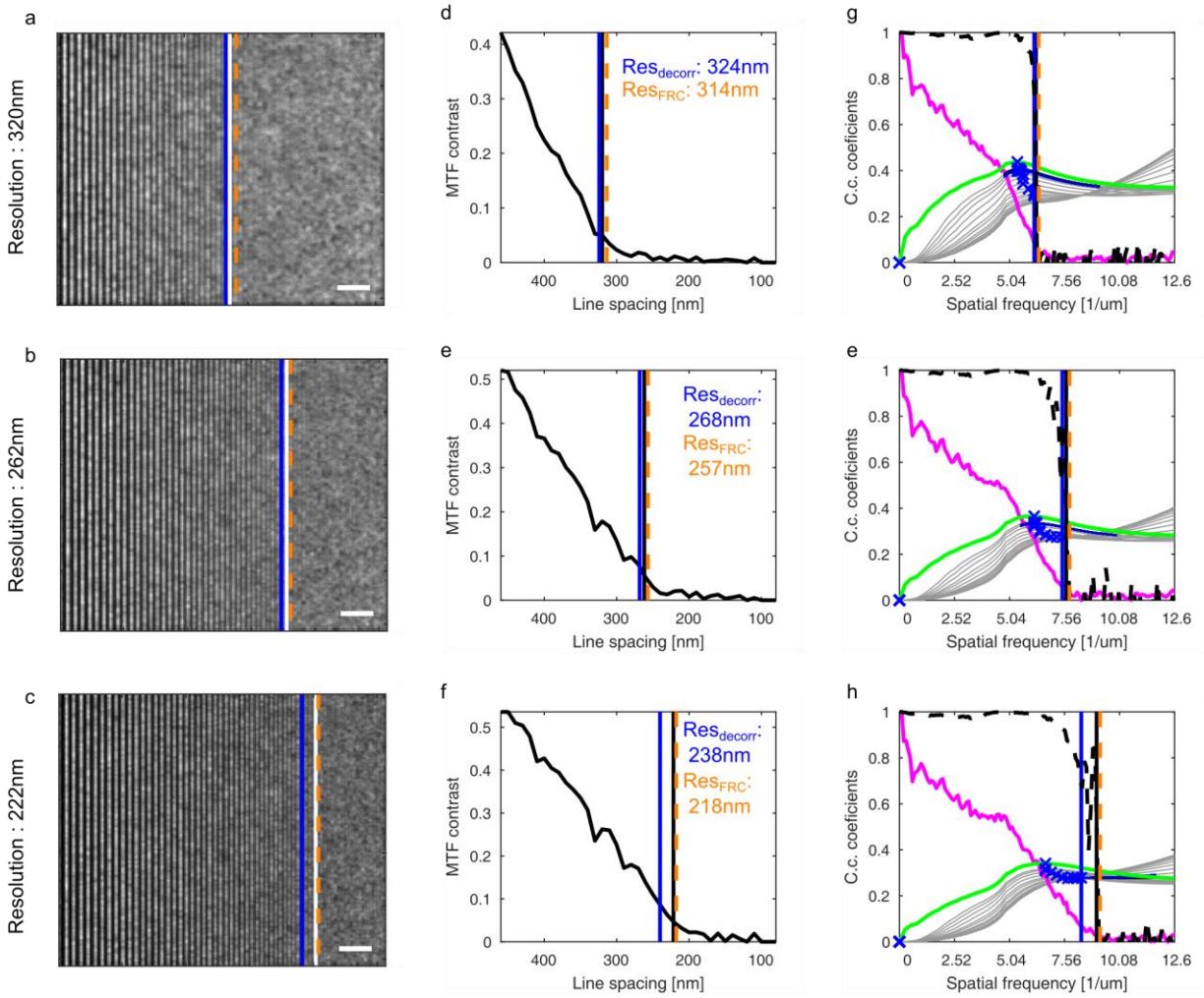

Figure S4 : MTF simulations and resolution estimation (a-c) Simulated MTF for 3 different resolutions (Blue line: max. resolution, Orange dashed line: FRC resolution, White line: Input resolution), Scale bar: 2um. (d-f) MTF curves extracted from (a-c). (g-i) Decorrelation analysis of (a-c) (Magenta line: Radial average of log of abs of the Fourier transform of (a-c), Green line: d0, Gray lines: all high-pass version of d, Black dashed line: FRC curve, Vertical blue line: estimated resolution, Orange dashed line: FRC resolution, Vertical black line: input resolution). Scale bar: 2um.

We simulated a widefield image of a dense (about 500 emitters per um^2 in average) distribution of point emitters forming an MTF pattern. We have a FOV of 20um and started with a period of 460nm up to 80nm, decreasing in steps of 10nm. Each period is repeated two times. Each point emitter contributes incoherently to the image intensity. We show in Fig. S4 (a-c) three MTF images of varying resolution (320, 262 and 222nm, corresponding to a NA of respectively 0.9, 1.1 and 1.3 for a wavelength of 576nm). The blue line denotes the estimated resolution and the white line the theoretical resolution. The FRC resolution (314, 257 and 218nm), obtained by computing the second image in identical conditions, is shown as an orange dashed line and is slightly over-estimating the theoretical resolution. We then compute MTF curves (Fig. S4d-f) by averaging along the direction perpendicular to the pattern and selecting adequate sub-windows for contrast computation. Again, we indicate the estimated resolution (blue line) and the theoretical resolution (black line). Fig. S4(g-i) shows the results of the decorrelation analysis.

2.3. Ring and sparse lines structures

We also simulated ring structures with an inner diameter ranging from 600 to 200nm and a width of 30nm. We set the theoretical resolution to be equal to the inner diameter of a ring. Each ring is constituted of 1000 molecules, resulting in about 10'000 to 40'000 emitters per um^2. We show in Figure S5a the resulting image. Interestingly, the ring with an inner diameter equal to the theoretical resolution cannot be resolved. This is due to the shape of the structure. The contribution of all the emitters actually decreases the contrast of the dip. This means that to be able to resolve a ring, one needs to have a resolution of a least two times the inner diameter. To confirm this effect, we show in Figure S5d-f sparse line structures with similar spacing as the rings, simulated under the exact same conditions. The lines with a spacing equal to the resolution are this time resolved. By computing another image, we measure an FRC resolution of 316nm.

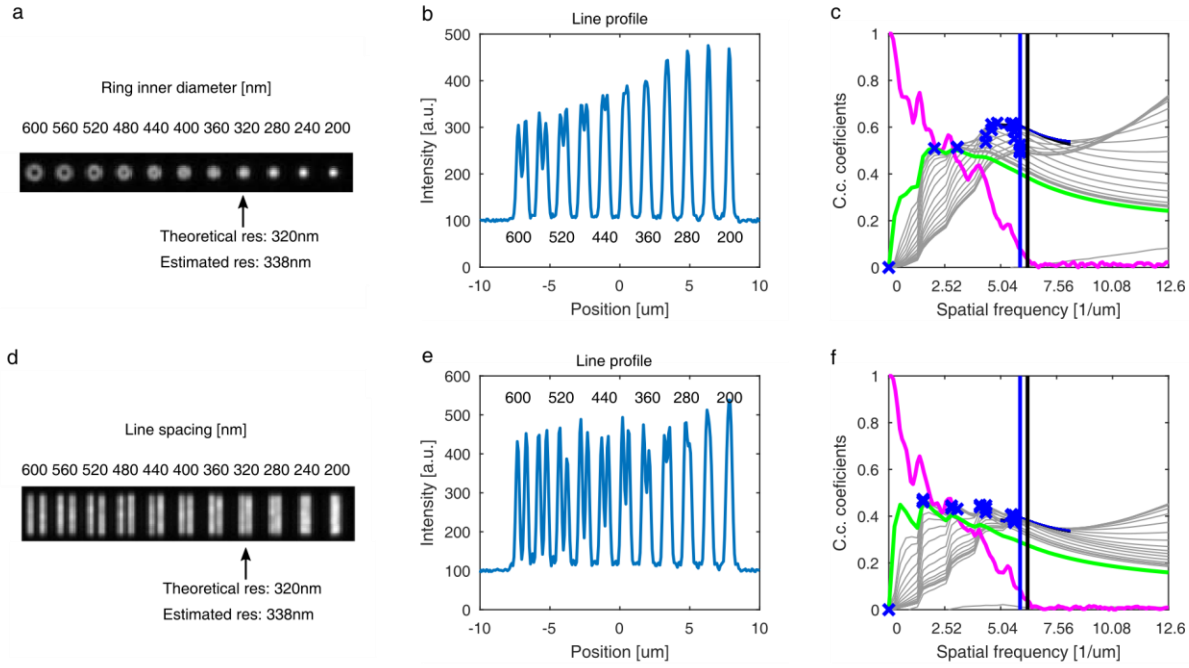

Figure S5 : Test objects in simulations. (a) The simulated intensity of ring structures (inner diameter of 600 to 200nm in steps of 40nm) with an input resolution of 320nm. (b) The line profile showing the decreases of the contrast in the ring centers. (c) Decorrelation analysis with an estimated resolution of 338nm. (d) The simulated intensity of sparse line structures with similar spacing and conditions. (e) The line profile showing the decreases of contrast with decreased spacing. (f) Corresponding decorrelation analysis with an estimated resolution of 338nms. Scale bar: 2um

2.4. Crossing lines

Finally, we simulated crossing lines (Fig. S6 a-c) as another structure of interest to quantify the validity of our resolution estimator. The structure consists in two 30nm width and 10um long lines crossing each other with an angle of 5°. Each line is made of 6000 randomly distributed emitters. With a theoretical resolution of 263nm, the algorithm independently estimated a resolution of 275nm, which is consistent with all the other simulations and what is expected from the theory. We repeated the simulation and changed the input numerical aperture from 0.5 to 1.4 NA (Fig. S6d). The estimated resolution (orange curve) follows precisely the theoretical resolution (solid blue curve). We also notice that, similar to the results obtained in Section 2.1, the estimated resolution is equal to about 1.1 times

the resolution as defined by Abbe. Our resolution estimator does not exhibit any structure dependent bias. By computing another image, we measure an FRC resolution of 256nm.

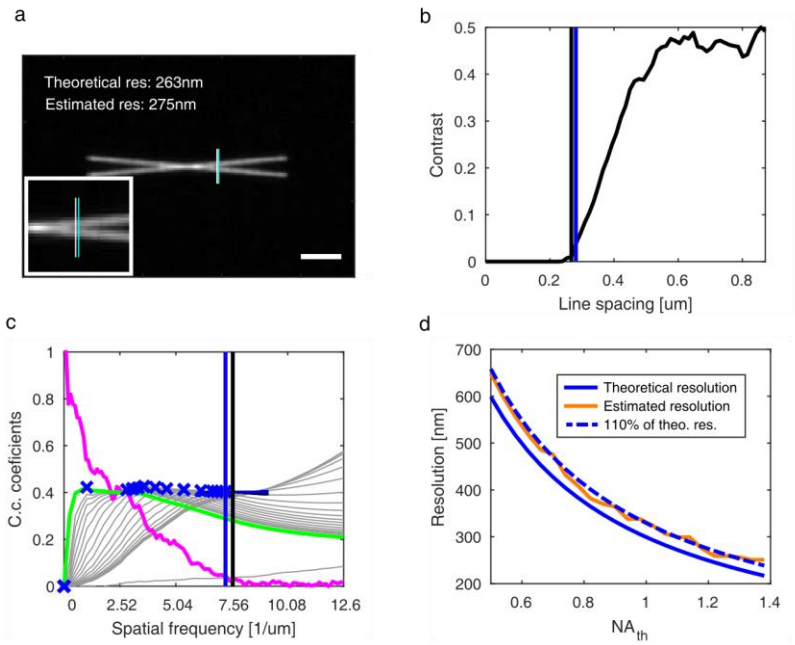

Figure S6: Decorrelation resolution estimation for crossing lines. (a) The simulated intensity of crossing lines with a theoretical resolution of 263nm and an estimated resolution of 275nm. The white and blue vertical lines indicate the position where the spacing between the two crossing lines is equal to the theoretical resolution (white line) and the estimated resolution (cyan line). (b) Contrast as a function of line spacing (Black line: Theoretical resolution, Blue line: Estimated resolution). (c) Corresponding decorrelation analysis with an estimated resolution of 275nm. (d) Resolution estimation for a theoretical NA ranging from 0.5 to 1.4 (Solid blue line: Theoretical resolution, Orange line: Estimated resolution, Dashed blue line: 110% of theoretical resolution). Scale bar: 2um

3. GATTAquant nanorulers

Due to their high reproducibility and nanometric accuracy, DNA origami have been proposed as calibration standards for resolution measurement in classical and super-resolution microscopy[1].

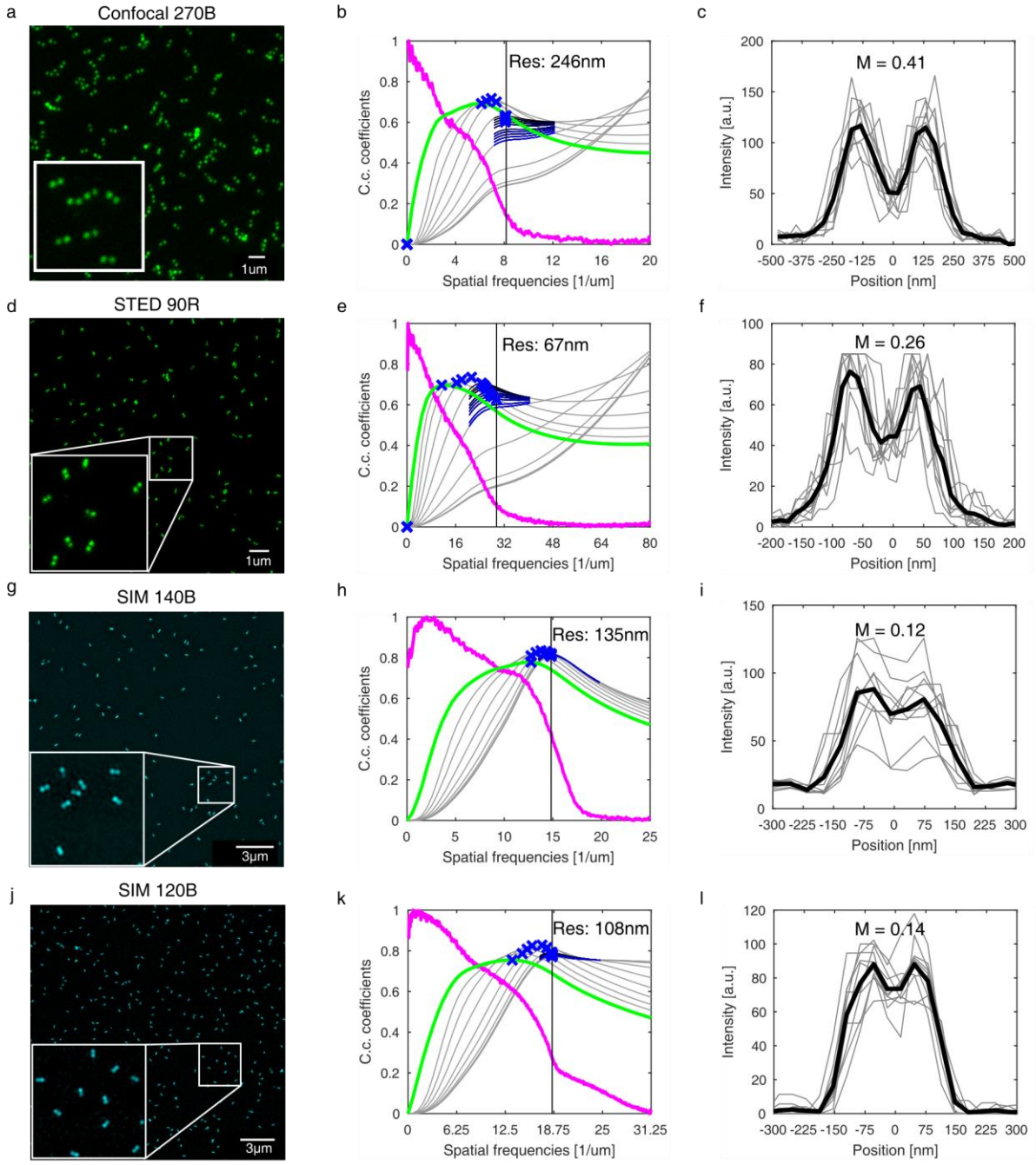

Figure S7: GATTAquant nanorulers and resolution estimate. (a-c) Confocal imaging. (d-f) STED imaging. (g-l) SIM imaging. (Left column) GATTAquant nanorulers images. Nanoruler type is indicated above the image, the number indicates the mark-to-mark distance in nm. (Middle column) Corresponding decorrelation analysis and resulting resolution. (Right column) Average (black line) lines profiles of 10 (gray lines) individual molecules and modulation contrast M. Image acquisition and sample details are provided in Table S2.

In order to demonstrate the validity and robustness of our method, we processed several datasets nanorulers directly provided by GATTAquant (courtesy of P. Tinnefeld and J. Schmied). Independently of the modality, the resolution estimate is in perfect agreement with the samples specifications and manually selected line profiles. We see that when the structure is properly resolved, as it is the case for confocal, STED and PAINT images, the resolution estimate is significantly smaller than the nanoruler size. For the two SIM images, the resolution estimate is much closer to the DNA origami size, which is consistent with the line profiles and contrast measurement, where the structure can barely be resolved.

For the PAINT data (see Fig. S8), we localized 10 molecules, co-aligned them and averaged them to get the resolution estimate. Particle-averaging methods widely used in *cryo-electron microscopy*, have been also adopted by researchers using SMLM . For example, several labs, working with hightroughput SMLM setups used, particle averging to elucidate labeled *protein organization in* structures such as of the nuclear pore complex[2] and centrioles[3]. We also computed the resolution over the whole field of view and obtained a resolution of 32nm using FRC and 45nm using our method. The difference between the particle averaged resolution and the whole FOV resolution can be attributed to sub-optimal co-alignment.

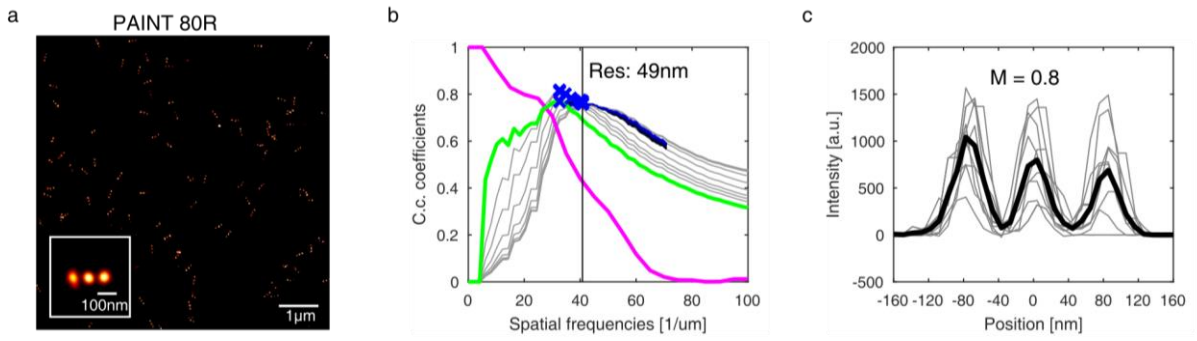

Figure S8: GATTAquant nanorulers and resolution estimate for PAINT microscopy. (a) PAINT image of nanoruler (inset: Average of 10 manually localized and co-aligned molecules). (b) Decorrelation analysis performed on the averaged image. (c) Line profile of inset of (a) and modulation contrast M. Image acquisition and sample details are provided in Table S2.

4. Bright-field data

In addition to fluorescence microscopy, our method can also be applied to partially coherent imaging.

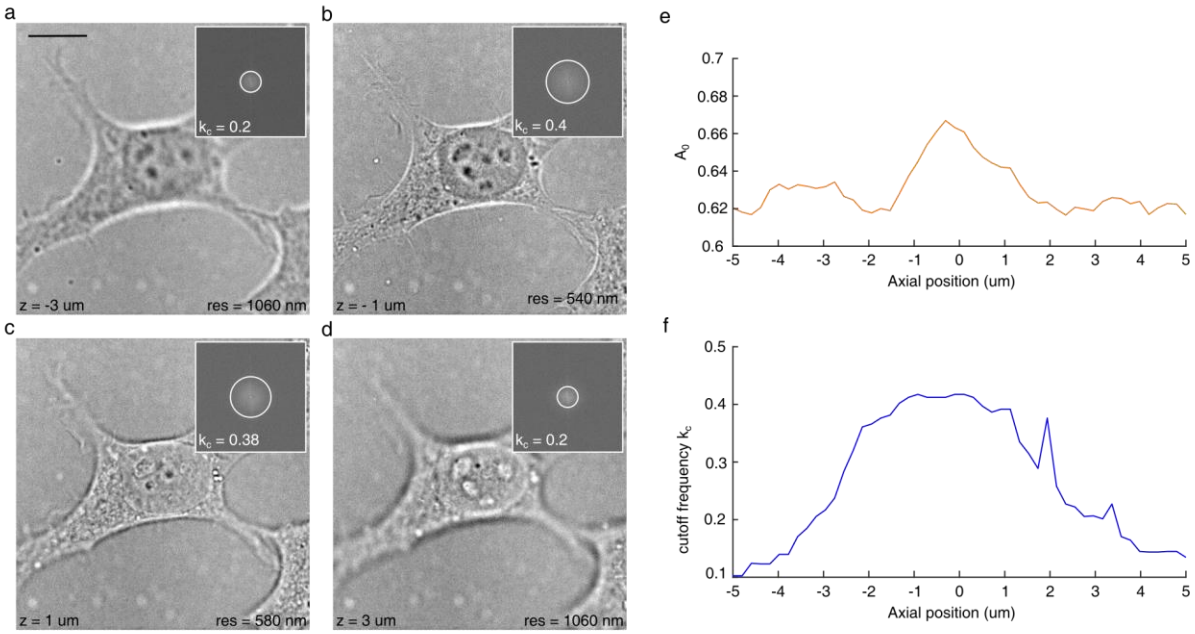

Figure S9: Bright field analysis (a-d) Selected slice of a 3D bright field stack of fixed HeLa cell (Inset: corresponding Fourier transform and estimated cutoff indicated by white circle). (e) A_0 as a function of the axial position. (f) Estimated cutoff frequency as a function of axial position. Scale bar, 5 µm. Image acquisition and sample details are provided in Table S2.

We processed a bright-field z-stack (50 slices, 200nm axial step size) of a fixed HeLa cell (Fig. S9 a-d)[4]. We see (Fig. S9e) that the SNR is maximal when the cell is in focus and well contrasted. The cutoff frequency estimate demonstrates the ability of the method to estimate the spatial frequency content. As we approach the focus, the cutoff frequency rises continuously until we reach the coverslip at around -2um. As we move through the cell, the resolution stays roughly constant, until it starts to drop at around 1um. The cutoff frequency peaks observed at 2 and 3.4um are due to highly scattering vesicles.

5. Fluorescent beads resolution

A typical way to assess the performance of a microscope is to image a single layer of fluorescent monodispersed beads. If the beads are sufficiently smaller than the system point-spread function and if the beads are well separated, a fit of the beads image can provide a good estimate of the microscope resolution in idealized conditions.

Here we demonstrate how our method performs on a technical sample (Tetraspeck beads, 175 nm).

Two large z-scan (10microns, steps of 25nm) were acquired (Fig S10, a-d), with 488 and 635nm excitation. As it can be seen, most of the beads formed clusters. This sample is therefore not suitable for fitting. Each frames were then processed with our algorithm to estimate the cutoff frequency.

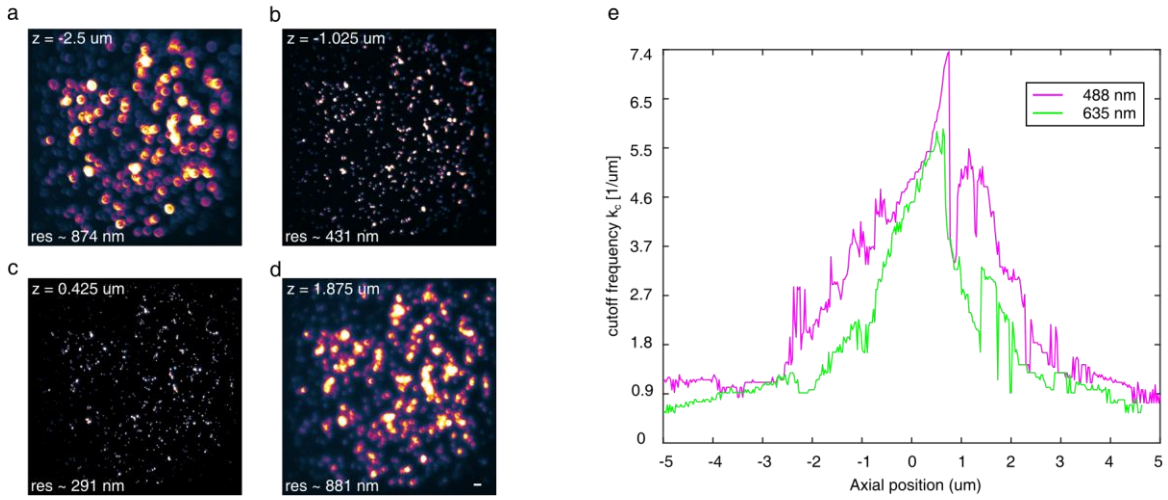

Figure S10: Resolution of fluorescent beads. (a-d) Images of Tetraspeck beads excited with 488nm excitation laser line at various axial positions. (e) Cutoff frequency estimate as function of the defocus for 488 (magenta) and 635nm (green) excitation. Scale bar, 5 µm. Image acquisition and sample details are provided in Table S2.

Fig. S10e shows how the cutoff frequency evolves through the z-scanning. As expected, the 488 excitation leads to an overall better resolution, independently of the z-position.

We measure the lowest resolution of 332nm with 640nm excitation and 276nm with 488 nm. Considering the size of the beads (175nm, which cannot be considered to be an ideal point emitter), the excitation wavelength and the objective NA (Nikon super-resolution water immersion 1.27NA), we can approximate the expected resolution as $res_{640} \sim \sqrt{256^2 + 175^2} = 310\ nm$ and $res_{488} \sim \sqrt{196^2 + 175^2} = 262\ nm$. Both measurements show good agreement with the theoretical value.

We observe the expected resolution is reached, but only on a very narrow 200nm range. The asymmetry of the cutoff as a function of z shown in Fig. S10e reflect the asymmetry of the point-spread function. Consequently, we propose our method as a practical way to test the performance of an objective lens and the alignment of a microscopy setup.

6. ImageJ plugin basic manual

In order to simplify the access to our method, we translated the algorithm in Java and developed an ImageJ plugin (publicly available on https://github.com/Ades91/ImDecorr.git; tested for ImageJ 1.48 to 1.52 and Micromanager 1.4). Fig. S11 shows the current plugin graphical user interface (GUI of Version 1.1.5).

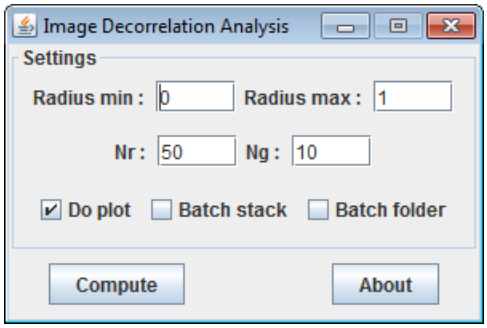

Figure S11: ImageJ plugin V1.1.5 with default settings

The operation mode of the plugin is straightforward. Open the image of interest in ImageJ and make sure it is the active window. Before running the analysis, it is important to set the image pixel size and units (Image -> Properties… -> Unit of length, Pixel width and pixel height). If empty or not defined, the plugin will return the resolution in pixel units. Click on compute and once the analysis is done, results are added to the main results table.

The plugin supports multidimensional stacks of any bit depth. If a RGB image is supplied, it will be automatically converted to grayscale. The plugin also supports rectangular ROI, which allows to repeat the analysis on sub-regions and check the consistency of the estimate over the whole image.

The settings panel is composed of 4 optional parameters of the computation, specifying the range of normalized frequencies where the correlations have to be computed (from Radius min to Radius max), as well as the number of points in between (N_r, typically 50 points). Finally, N_g (typically 10) specify the number of intermediate high-pass filtering used to find the resolution. These parameters essentially determine the speed of the computation. Since all the points of the decorrelation function are independent of each other, the computation time is proportional to the total number of points which is equal to $N_r * (2 * N_g + 1)$. The proposed default value of $N_r = 50$ and $N_g = 10$ were experimentally determined as good compromise for fast but accurate results.

We also provide additional processing options in the form of 3 check-boxes:

Do plot:

If checked, plot all the computed decorrelation functions and local maxima (example of plot shown in Fig. S12).

Batch stack:

If checked, process all the frames, slices and channel of the current image. If do plot is also checked, all the decorrelation functions for all the images will be plotted.

Batch folder:

If checked, the user will be asked to select a folder containing images. All images are then opened, processed and the result table is automatically saved in the selected folder as a .csv file. Again, if "do plot" is checked, all the decorrelation analysis will be plotted.

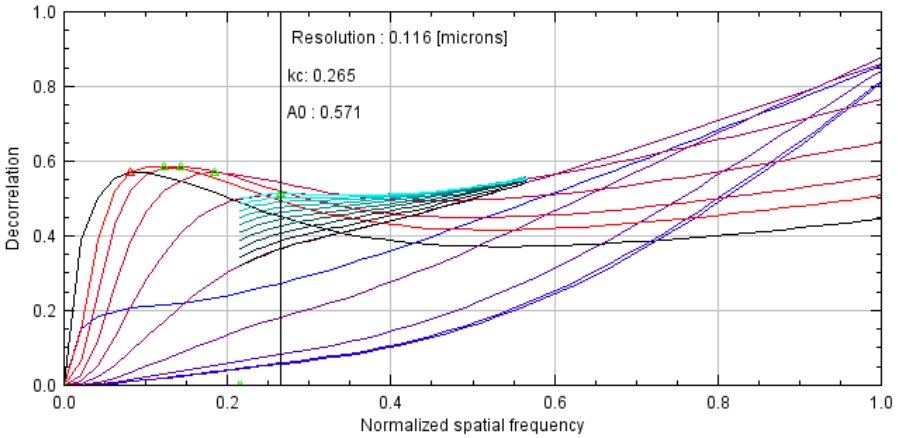

Figure S12: ImageJ plot of the analysis showing the non-filtered decorrelation function(black), its local maximum (red triangle), all the high-pass versions (color gradient from red (weak filtering) to blue (strong filtering)), all the local maxima (green triangle) and the estimated resolution, cutoff frequency kc and SNR A0. The second set of lines (here from ~ 0.15 to 0.52) corresponds to the refinement operation where the computation is repeated on a smaller range of N_r and N_g for increased robustness.

7. Detailed STED plots and additional STED experiments

Figure S13a shows the evolution of the non-filtered decorrelation function d_0 used for SNR estimation for the STED data in Fig. 2e-f. We clearly see that as the frame number increases (magenta to green), the peak amplitude drops. If we continued the imaging, the peak would have eventually vanished as the function will tend towards a straight line. Figure S13b-f shows the full decorrelation analysis of STED for 5 different relative depletion powers for Fig. 2g-h. We see that at 0%, the resolution is that of a normal confocal. As we increase the STED power, the resolution improves as expected. We observe no significant improvement in resolution between 60 and 80%. The ideal relative STED power is then estimated between 40 and 60%.

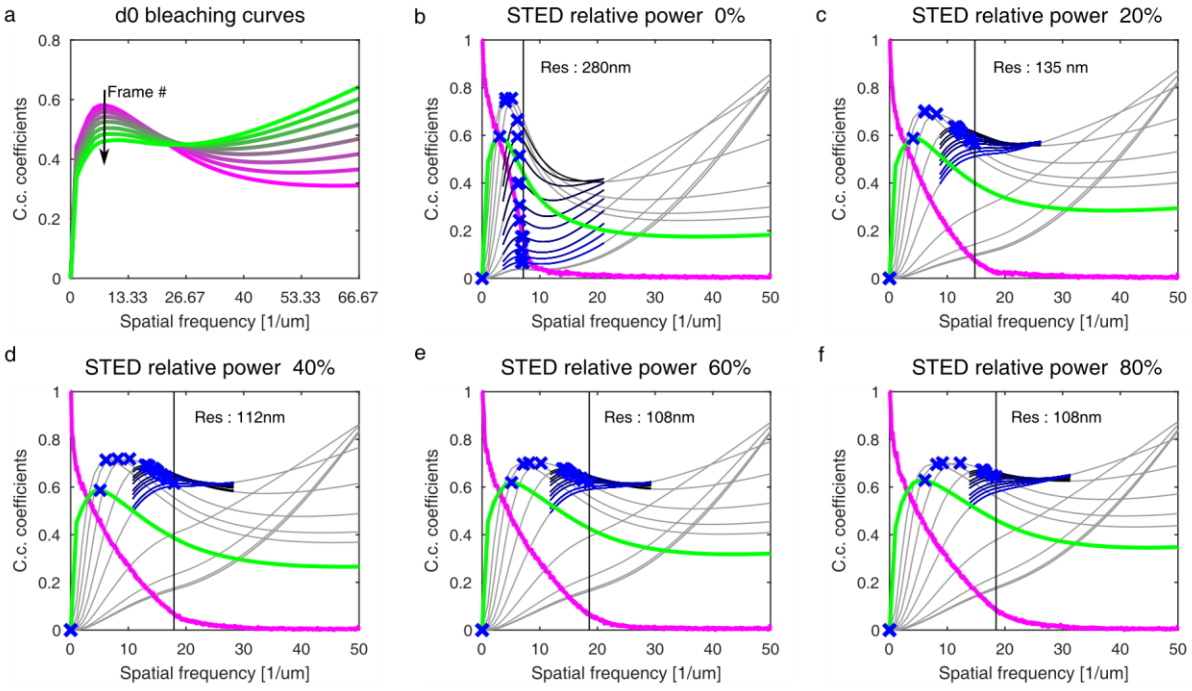

Figure S13: Detailed decorrelation functions for STED. The data corresponds to Figure 2g,h. (a) Non-filtered decorrelation function d0 of repeated STED imaging. (b-f) Decorrelation analysis of STED images with varying relative STED power ranging from 0-80%

In order to further demonstrate the practical use of our algorithm for quick and robust assessment of microscopy performances, we acquired and processed several additional STED and confocal data, investigating the huge parameter space (STED power, dyes, excitation wavelength, STED delay, etc..) associated with any microscopy experiment. We show in Figure S14a how the resolution improves as a function of the STED beam intensity for COS7 microtubules labelled with Atto594. We observe that the maximum resolution is reached at about 40 to 60% of relative STED power. Further increases in the STED power has even a detrimental effect on the resolution. Similar experiments were done with Atto940LS. We see (Figure S14b) that the optimal STED power now lies in between 80 to 100% of relative STED power. Figure S14c shows representative data of Figure S14b. We show in Figure S14d that the confocal resolution estimate does not significantly depend on the pixel size. Another crucial parameter for STED imaging is the delay between the excitation and depletion of the fluorophores. An incorrect pulse synchronization will result in less efficient depletion and significantly impact the final image resolution.

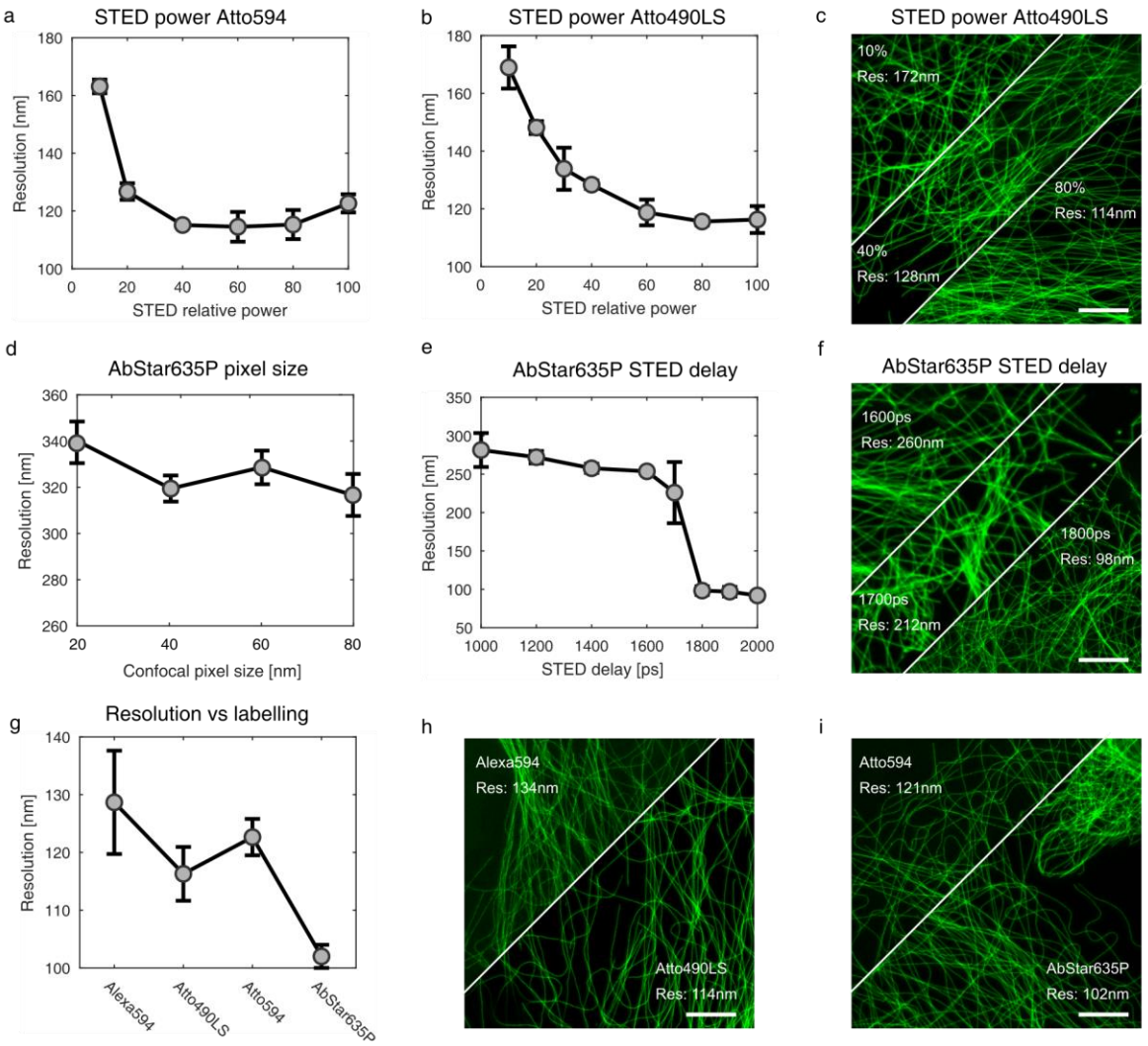

Figure S14 : Additional STED experiments (a) Resolution vs STED power for Atto594 labelling. (b) Resolution vs STED power for Atto490LS labelling. (c) Representative STED images for 10, 40 and 80% STED power for the data in (b). (d) Confocal resolution vs pixel size for AbberiorStar 635P labelling (short: AbStar635P). (e) Resolution vs added delay between the excitation and STED laser pulse for AbberiorStar 635P labelling. (f) Representative STED images for 1600, 1700 and 1800ps STED delay for the data in (e). (g) STED resolution for different labelling at 100% STED power. Alexa594 is short for Alexa Fluor 594. (h-i) Representative images of STED for different labelling for the data in (g). Image acquisition and sample details are provided in Table S2.

We show in Figure S14e the resolution as a function of the STED delay and corresponding representative data in Figure S14f. We see that an added delay of at least 1800ps is required in order to reach the optimal STED regime.

Finally, we also show in Fig. S14g how the resolution varies as a function of the dye. Fig. S14h and S14i show representative images.

8. *Sectorial resolution estimation*

The proposed method is very flexible and can be easily translated into higher dimensions. In order to estimate the sectorial and axial resolution, the shape of the mask has to be adjusted. Fig. S15a shows another STED image of the microtubules. The Fourier transform of (a) is shown in Fig. S15b and reveals a clear asymmetry of the Fourier spectrum. The dashed white circle represents the resolution estimated by our method when applied to the whole image. In order measure the resolution as a function of the direction, the shape of the mask as to be adjusted. Fig. S15c indicates how the circular mask has to be segmented in order to estimate the sectorial resolution in 8 directions. In this case, a total of 8 sectors (S1-S8) are defined and a standard decorrelation analysis is performed for each sector.

Fig. S15d shows the resolution dependent cutoff frequency (dashed white line), correctly measuring the anisotropy of the Fourier spectrum.

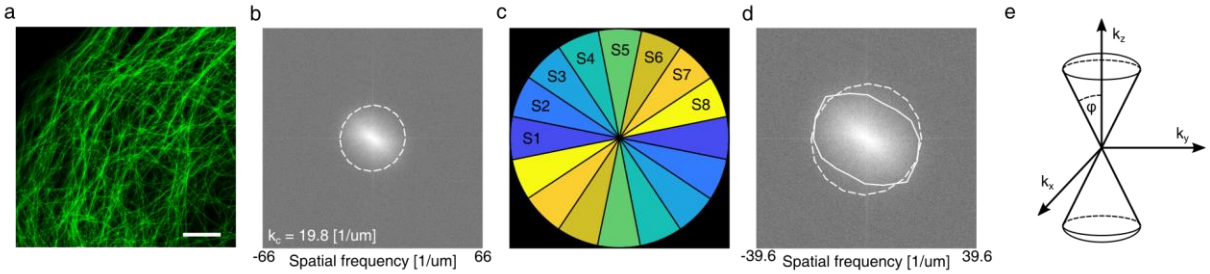

Figure S15: Sectorial and axial resolution (a) Example image. (b) log of abs of Fourier transform of (a) indicating the average resolution as a white dashed circle. (c) Shape of the masks used for the sectorial resolution estimation in 8 directions. (d) Sectorial resolution estimate (solid line) and average resolution (dashed circle). (e) Theoretical shape of the 3D mask required in order to estimate axial resolution. Scale bar, 5 µm. Image acquisition and sample details are provided in Table S2.

Fig. S15e illustrates the shape of the mask required for axial resolution estimation. The parameter φ is the angle of the cone oriented along the z-direction and defines the trade-off between the selectivity of the mask and the noise (small φ means good selectivity but few data points leading to a noisy estimate, large φ means poor selectivity but more robust estimate). The extension of the algorithm to 3D requires to move from polar to spherical coordinate. Another strategy for the estimation of z-resolution could be based on the computation, for all x and y position, of a 1D decorrelation function along the z-axis. This will result in a 2D image, containing the cutoff frequency estimate for each point. A histogram analysis may be used to determine which resolution was the most prominent, providing an alternative mean to assess the axial resolution with ideal selectivity of the z-resolution. However, this question requires further work, investigating for example the effect of a limited number of z-plane.

9. Compatible SIM reconstruction

Due to the sensibility of the method to manipulations of the Fourier space, publicly available SIM reconstructions algorithms are not compatible with our method without resulting in biased resolution due to Fourier filtering and deconvolution.

Consequently, we wrote our own SIM reconstruction algorithm (in Matlab) and discuss required features for decorrelation compatible SIM reconstruction.

I. Pre-processing

We first compute and subtract the mean of all images. We then apodize the edges of the all the raw image with a cosine function and add the previously computed mean. High frequency artefacts arising for edges discontinuities are consequently minimized.

II. Peak finding

After specification of the frequency band where the peak should be found, the absolute value of the Fourier transform of all the raw images are multiplied with a circular symmetric inverted OTF, defined as

$$OTF_{inv}(k) = \left(\frac{|k|}{k_c}\right)(|k| < k_c) \tag{S17}$$

where $k = \sqrt{k_x^2 + k_y^2}$ is the radial frequency and k_c is a user defined cutoff frequency. This operation attempts to flatten the Fourier space by balancing the effect of the OTF on the peaks intensity. Consequently, the 5 largest Fourier pixel within the frequency band are localized and clustered. This allows to reliably exclude randomly bright Fourier pixels. The position and phase of the peak are then stored.

III. Unmixing

Using the peaks phase values, an adequate transformation matrix is build and the corresponding Fourier components are unmixed pixels per pixels for each angle.

IV. Reconstruction

For each angle, all the zero order components are averaged to reconstruct the pseudo wide field image. This image is then zero-padded in Fourier space and all the other components are translated according to their peak position and added together. The resulting Fourier spectrum is then reweighted to balance the partial overlap of the Fourier components (otherwise, the Fourier space of the SIM image will be plagued with weak edges that might produce significant peaks in the decorrelation analysis, preventing any resolution estimate).

Finally, instead of masking the Fourier space with an apodization filter, that might bias the resolution estimate (see Supplementary Material, Section 11), we crop the Fourier space. This partially removes the high-frequency noise but without creating any artificial edges. This also have the side effect of changing the projected pixel size of the resulting SIM image.

10. Deconvolution and post-processing

In the following section, we discuss and illustrate issues arising when applying various post-processing algorithm prior to the decorrelation analysis.

First we show in Fig. S16a, 3rd order raw SOFI image of microtubule network labelled with Alexa647. The Fourier transform is shown in the inset. Fig. S16b shows its corresponding decorrelation function. Fig. S16c shows the same image after a basic Fourier filtering operation. In this case, a simple binary mask with a normalized radius of 0.6 has been applied. While the image looks almost identical to the original, the decorrelation analysis is strongly affected by this artificial operation. It interprets the mask as a transfer function. In this very specific case, the mask does not affect the shape of the function near the real cutoff frequency so one could circumvent the issue by only computing the curve up to the spatial frequency 0.5 for example (Radius max. = 0.5 in the case of the imageJ plugin). However, if the mask is closer to the cutoff, this simple trick is likely to fail and no resolution estimate could be performed on such image.

Fig. S16e shows the same image, after Lucy-Richardson deconvolution (Matlab R2017b "deconvlucy") with various input Gaussian PSF FWHM (ranging from 108 to 238nm). The decorrelation analysis shows very drastic changes where the resolution goes from 288 to 100 nm. Fig. S16f shows their corresponding Fourier transform, where the effect of deconvolution is now clearly visible (10 iterations of LR, psf FWHM of 238, 180 and 108nm respectively). Fig. S16g shows the resolution estimate of the same image for different FWHM and number of iterations of Lucy-Richardson deconvolution.

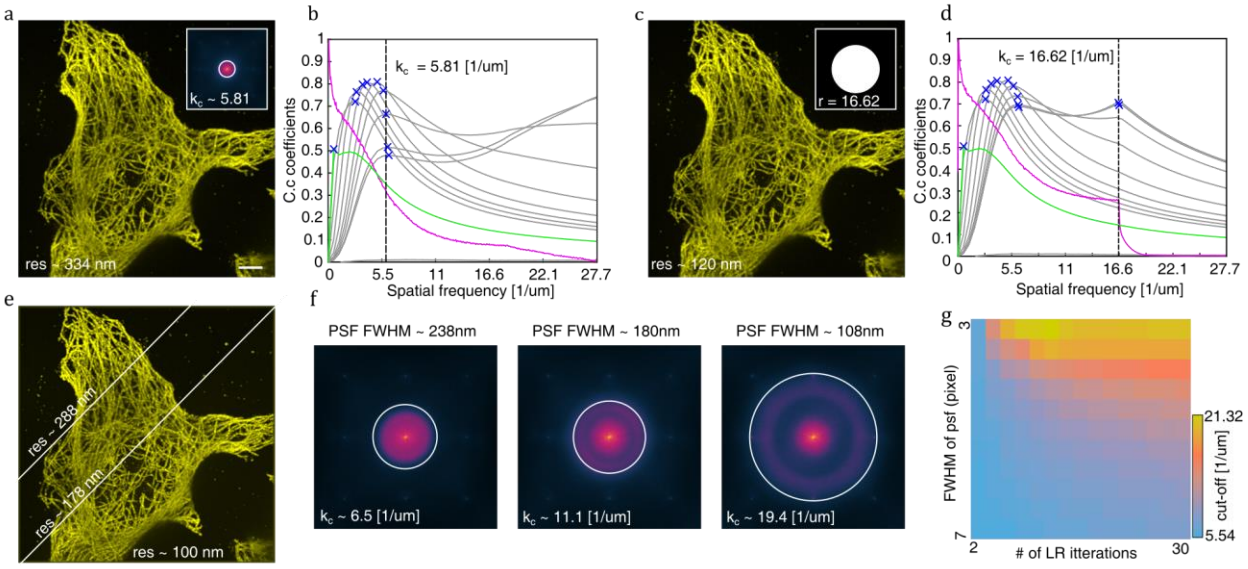

Figure S16: Fourier filtering and deconvolution (a) Raw SOFI 3 images and its Fourier transform in inset. (b) Corresponding decorrelation analysis. (c) Fourier filtered version of (a) with the used mask in inset. (d) Corresponding decorrelation analysis, showing incorrect result due to the artificial intervention. (e) Lucy-Richardson deconvolution using 20 iterations and a FWHM of 238, 180 and 108nm. (f) Corresponding Fourier transform, showing how the deconvolution modified the frequency spectra and the resolution estimate. (g) Resolution estimation for various FWHM and number of iterations of LR deconvolution. Scale bar, 5 µm. Image acquisition and sample details are provided in Table S2.

It demonstrates that the resolution can be artificially set to any value. **We here have to mention that we never recommend to blindly deconvolve an image and that proper deconvolution ideally requires an experimentally acquired point-spread function**. The purpose of this section is just to demonstrate how ANY deconvolution will influence, in general, our method. This means that our algorithm can be used as a tool to quantify the deconvolution strength and also to estimate the ideal number of iterations but not check the validity of the deconvolution.

In addition to Fourier filtering and deconvolution, there are also several sources of artificial high-frequencies that we came across during the development of the algorithm. This is a non-exhaustive list of common practice that may hinder the ability of the algorithm to estimate the resolution:

- Removing negative values by applying a threshold creates local non-linearity, adding a high-frequency signal to the image.
- Background subtraction algorithms (especially morphological operation based such as the rolling-ball algorithm) are prone to produce high-frequency artefacts.
- Camera lines artefacts or fixed pattern noise are very-high frequency signals that might lead to overestimation of the resolution. The camera pattern should be characterized and used to pre-normalize the image.
- Image up-sampling/down-sampling, in real space or via Fourier zero-padding, should be avoided.
- Small images are more vulnerable to noisy peaks in the decorrelation analysis (256x256 is usually large enough).
- Quantization error when changing the bit-depth of the data may introduce edges all over the image, which can result in wrong estimate. The images should be normalized to the full bit-depth prior to quantization.

11. *Single Molecule Localization Microscopy simulations*

To confirm that our algorithm is also able to estimate the resolution of localization based image, we conducted simulations. The simulation consists in a total of 16000 point emitters forming a regular pattern of pair of lines with decreasing spacing, starting from 128nm to 8nm (see Fig. S17a). Each line is 400nm long and 2nm wide, corresponding to a density of 625'000 molecules per um^2. The effect of diffraction and of the limited numerical aperture is simulated by convolving the point emitters (represented on an oversampled grid with an up-sampled pixel size of 1nm) with an incoherent 2D airy function (corresponding to a wide field resolution of 215nm) of integrated intensity I_{ON} determining the average number of photons per frame and per emitters. The blinking required for the localization of the emitter is simulated by a Markovian process where the ON time (number of frames where the molecule emits photons), the OFF time (number of frames where the molecule does not emit photons) and the bleaching time (number of frames before the molecule is not able to emit photons anymore) all follow an inverse exponential law of characteristic time $T_{ON} = 2, T_{OFF} = 1000$ and $T_{bl} = 2000$. Therefore, at each frame and for a total of 1000 frames, only a sparse subset of emitters contributes to the signal intensity, typical for SMLM. The final camera signal is then obtained by adding shot noise and a Gaussian background noise (Fig. S17b). The molecules are then localized using ThunderSTORM[5] and rendered in Matlab by replacing each localization by a Gaussian of standard deviation equal to the localization uncertainty[6,7] (Fig. S17c) that we compute in Matlab.

Each pair of lines are then isolated and averaged along their major orientation (Fig. S17d), which allows us to compute the contrast between the maximum intensity I_{max} and the intensity in the dip between the two lines I_{dip}, defined as $M = \frac{I_{max} - I_{dip}}{I_{max} + I_{dip}}$. By repeating this computation for all the sub-structures, we are able to compute an effective Modulation Transfer Function (MTF), which provide an objective way to determine the resolution of the reconstructed image (Fig. S17e). We see that as the spacing between the lines diminishes, the contrast drops almost linearly. We then define the resolution of the image to be the

intersection of the MTF with the threshold 0.1, which corresponds to the modulation contrast of two point emitters spaced by a distance equal to the resolution as defined by Abbe. We obtain an effective resolution of 32nm.

We then use our algorithm on the reconstructed image (Fig. S17c) and compare its value with the effective resolution. Our algorithm estimates a resolution of 36nm (Fig. S17e, green dashed line), which is in perfect agreement with the previous simulations (see Section 2). The resolution estimate provided by the FRC metric and a threshold of 0.143 predicts a resolution of 27nm, which is more optimistic estimate as it corresponds to a contrast of 0, consistent with the literature[8].

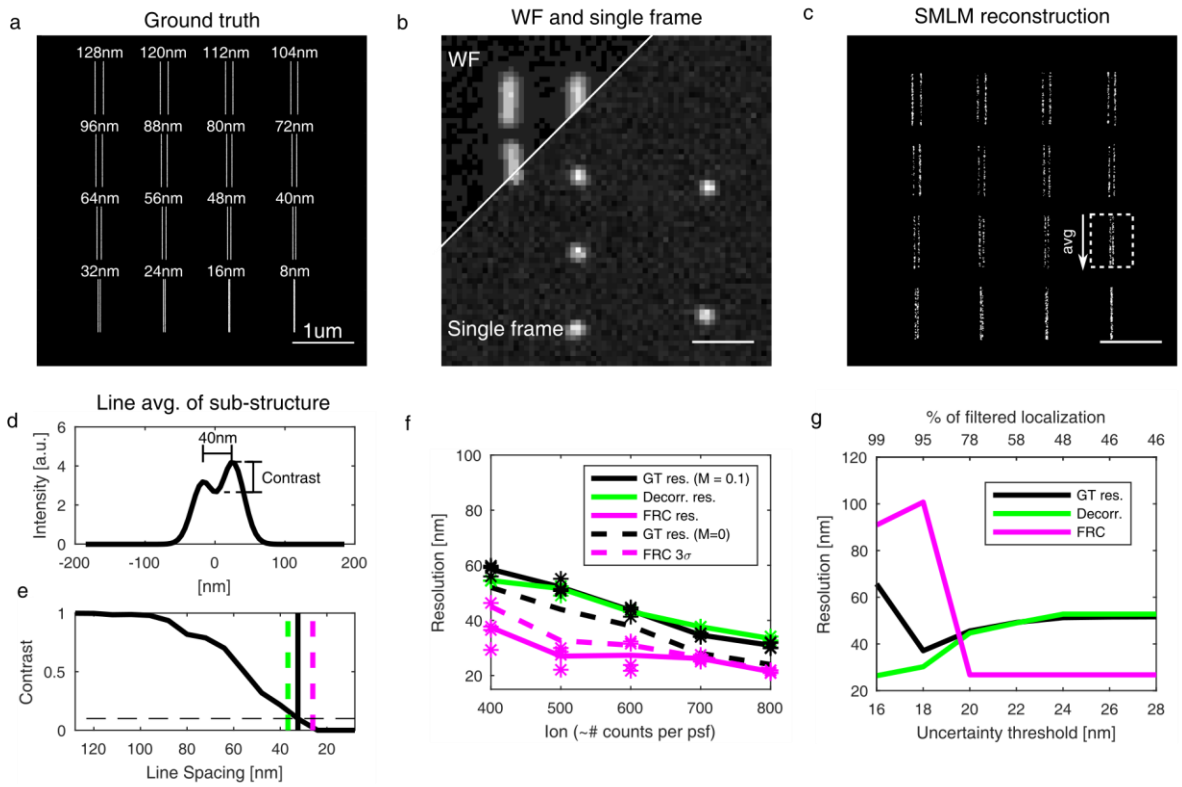

Figure S17 Simulations of Localization microscopy. (a) Spatial distribution of point emitters forming a series of lines with decreasing spacing from 128 to 8nm. (b) Temporal average (wide field) and single-frame of blinking emitters. (c) SMLM reconstruction using ThunderSTORM and Matlab; the dashed rectangle indicates the selection of a sub-structure and the arrow the direction of averaging. (d) Intensity profile of the sub-structure indicated in (c). (e) Contrast as a function of the line spacing for the image shown in (c); vertical black line: Ground truth resolution, green dashed line: decorrelation resolution, magenta dashed line: FRC resolution. (f) Ground truth resolution (black line: M=0.1, dashed black line: M=0), decorrelation resolution (green line) and FRC resolution (magenta line: 0.143 threshold, dashed magenta line: 3σ) as a function of I_{ON} for various T_{OFF} (the lines are showing the mean resolution over T_{OFF}; stars are showing the data points for the GT res, decorr. res. and FRC res.). (g) Ground truth (black line), decorrelation resolution (green line) and FRC resolution (magenta line) as a function of the uncertainty threshold.

We repeated the simulations by varying the number of counts per point spread function (via adequate tuning of I_{ON}) and keeping the background noise constant. For each I_{ON}, we varied the off-time T_{OFF} from 500 to 1250 in steps of 250, effectively changing the average number of emitters ON per frames from 34 to 14 and the average number of blinks per emitters from 0.98 to 0.38. For each reconstructed image, we then computed (Fig. S17f) the Ground Truth (GT) resolution from the MTF for $M = 0.1$ (solid black line) and $M = 0$ (dashed black line), the resolution using the decorrelation analysis (solid green line) and the FRC resolution using the 0.143 threshold (solid magenta line) and using the 3σ criterion (dashed magenta

line). We see that both methods are able to pick up the resolution improvement due to the higher number of photons per psf. However, we also see that our estimate is in good agreement with the ground truth resolution estimate, while both FRC criteria overshoots the ground truth resolution with $M = 0$.

We also show (Fig. S17g) how both algorithm performs as a function of the uncertainty threshold imposed on the localization prior to rendering. We filter any localization event with an uncertainty greater than the uncertainty threshold. We see from the ground truth resolution that as we remove poorly localized events, we indeed improve our ability to resolve the fine structures in the image. Our algorithm is also able to pick up this trend. We do however observe a clear difference of behavior when removing more than 78% of the total localization. In this case, the FRC resolution jumps to about 100nm while our resolution estimate drops below the ground truth resolution. This behavior is due to the difference in how the two algorithms try to estimate the resolution. FRC is based on splitting the localization in two stochastically independent subsets. If the number of localization is too low, the two images cannot correlate and thus the algorithm predicts a deterioration in resolution. On the other hand, the decorrelation analysis, which works on a single image will have a completely opposite prediction. All the algorithm see is a sparse distribution of very high-frequency Gaussians. The corresponding resolution in terms of Fourier space frequency content is therefore over-estimated.

Finally, FRC resolution estimate has been shown to be sensitive to multiple blinking events as they are prone to introduce spurious correlations, which leads to an overestimated resolution[9]. While it is possible to compensate for this effect by estimating the spurious correlation factor Q from the reweighted numerator of the FRC, it is not easily applicable when the blinking statistic is not precisely known. We performed simulations with added multiple blinking events. All fluorescent emitters that just turned OFF has a certain probability, controlled by the number pMB (probability of multiple blinking), to switch ON again. We show in Fig. S18a the log of the histogram of number of blinking events per molecule for different pMB. As expected, the larger the probability, the more a molecule is likely to blink during the same amount of time (1000 frames). We also show in Fig. S18b the resolution estimation as a function of pMB. We see that the FRC resolution (orange line) estimation gets lower with the probability due to increasing spurious correlations. In contrast, we see that our estimate (blue line) as well as the ground-truth resolution estimate (black line) are insensitive to the probability of multiple blinking events.

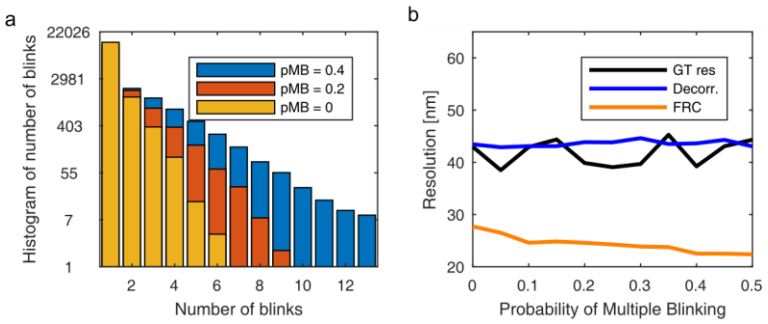

Figure S18 Resolution estimation vs multiple blinking. (a) Histogram of number of blinking events for three different values of probabilities of multiple blinking (pMB) on a logarithmic scale. (b) Ground-truth (black line), decorrelation (blue line) and FRC (orange line) resolution as a function of the probability of multiple blinking

Table S1: Summary of sample preparation, imaging conditions and buffer used for Figure 1 to 5

Figure	sample	sample preparation	imaging conditions	buffer
1a	COS-7 microtubules-Abberior Star 635P	COS-7 fixation and labeling, primary anti-tubulin antibody clone B-5-1-2 ascites fluid 1:200 dilution (Sigma-Aldrich), secondary goat anti-mouse-AbberiorStar635P 0.01 mg ml^{-1} (Abberior)	Leica TCS SP8 3X, 11.2 µW 634 nm illumination laser, 201.5 mW 775 nm STED laser, HyD: 645-720 nm, gain 100, pixel size 15nm binned 2x, 8x average, 200 Hz, gate 0.2-12	Mowiol-DABCO
2a, b	COS-7 microtubules-Abberior Star 635P	See above	Leica TCS SP8 3X, 2.25 µW 634nm illumination laser, HyD: 645-720nm, gain 100, pixel size 15nm binned 2x, 200 Hz, gate 1-11ns	Mowiol-DABCO
2c, d	COS-7 microtubules-Abberior Star 635P	See above	Leica TCS SP8 3X, 11.2 µW 634 nm illumination laser, 775 nm 201.5 mW STED laser, HyD: 645-720 nm, gain 100, pixel size 15 nm binned 2x, 8x average, 200 Hz, gate 1-11 ns	Mowiol-DABCO
2e, f	COS-7 microtubules-Abberior Star 635P	COS-7 fixation and labeling, primary anti-tubulin antibody clone B-5-1-2 ascites fluid 1:200 dilution (Sigma-Aldrich), secondary goat anti-mouse-AbberiorStar635P 0.005 mg ml^{-1} (Abberior)	Leica TCS SP8 3X, 179.2 µW 634 nm, 403 mW 775 nm STED laser, HyD: 645-720 nm, gain 100, pixel size 20 nm binned 2x, 8x average, 200 Hz, gate 0.8-11 ns	Mowiol-DABCO
2g, h	COS-7 microtubules-Abberior Star 635P	See above	Leica TCS SP8 3X, 634 nm 89.6-179.2 µW/22.4 µW illumination laser, 81-403 mW/0 mW 775nm STED laser, HyD: 645-720nm, gain 100, pixel size 20 nm binned 2x, 8x average, 200 Hz, gate 0.8-11 ns	Mowiol-DABCO
3a, b	U2OS cells actin-Atto 488	Huser lab, U2OS cells staining with phalloidin-Atto488, for details see ref 26 and https://www.fairsim.org/	GE Healthcare Delta-Vision|OMX v4, pseudo widefield average of SIM, for details see ref 26 and https://www.fairsim.org/	

3c, d	U2OS cells actin-Atto 488	See above	GE Healthcare Delta-Vision|OMX v4, SIM illumination, for details see ref 26 and https://www.fairsim.org/	
3e-h	U2OS cells mitochondria-mitotracker	Sauer lab, U2OS cells mitochondria-mitotracker, for details see ref 26 https://www.fairsim.org/	Zeiss Elyra S1, SIM illumination, for details see ref 26 and https://www.fairsim.org/	
4a	MEF cells paxillin-mEos2	Radenovic lab, MEF cells expressing paxillin labelled with mEos2, for details see ref 29	home-built TIRF microscope, for details see ref 29	
4b-e	HeLa cells microtubules-Alexa Fluor 647	HeLa fixation and labeling, primary anti-tubulin antibody clone DM1A 1:150 dilution (Abcam), donkey anti-mouse-Alexa Fluor 647 antibody 0.005 mg ml^{-1} (Invitrogen)	home-built widefield microscope, for details see materials & methods, excitation 635nm 1.9 kW cm^{-2}, 20 ms exposure time	50 mM MEA in 50 mM Tris-HCl pH 8.0 with oxygen scavenging, for details see materials & methods
4f	HeLa cells wheat germ agglutinin-Atto 565	HeLa fixation and labeling, wheat germ agglutinin-Atto 565 5 ng ml^{-1}, see Preparation of labeled proteins in materials & methods	home-built widefield microscope, for details see materials & methods, excitation 561nm 1 kW cm^{-2}	See above
5a-e	COS-7 microtubules-Abberior Flip 565	COS-7 fixation and labeling, primary anti-tubulin antibody clone B-5-1-2 ascites fluid 1:200 dilution (Sigma-Aldrich), secondary donkey anti-mouse-Abberior Flip 565 1:100 dilution, see Preparation of labeled proteins in materials & methods	home-built widefield microscope, for details see materials & methods, excitation 561nm 0.2 kW cm^{-2}, 20 ms exposure time	PBS, pH 7.4
5	GATTAquant PAINT HiRes 40R nanoruler	Courtesy of P. Tinnefeld and J. Schmied http://www.gattaquant.com/		

Table S2: Summary of sample preparation, imaging conditions and buffer used for Figures S2 to S16

Figure	sample	sample preparation	imaging conditions	buffer
S2	COS-7 microtubules-Abberior Star 635P same as 2c	COS-7 fixation and labeling, primary anti-tubulin antibody clone B-5-1-2 ascites fluid 1:200 dilution (Sigma-Aldrich), secondary goat anti-mouse-AbberiorStar635P 0.01 mg ml^{-1} (Abberior)	Leica TCS SP8 3X, 11.2 µW 634 nm illumination laser, 775 nm 201.5 mW STED laser, HyD: 645-720 nm, gain 100, pixel size 15 nm binned 2x, 8x average, gate 1-11 ns	Mowiol-DABCO
S7a-c	GATTAquant Confocal 270B	Courtesy of P. Tinnefeld and J. Schmied http://www.gattaquant.com/		
S7d-f	GATTAquant STED 90R	See above		
S7g-i	GATTAquant SIM 140B	See above		
S7j-l	GATTAquant SIM 120 B	See above		
S8	GATTAquant PAINT 80R	See above		
S9	HeLa cell	Fixed, unlabelled HeLa cell, data same as figure 2 ref[4]	Home-built widefield multi-plane microscope, for details see ref[4]	PBS
S10	Fluorescent beads	Tetraspeck beads, 175 nm	Home-built widefield microscope (NA=1.27, image pixel size=108nm)	
S14a,g,i	COS-7 microtubules-Atto594	COS-7 fixation and labeling, primary anti-tubulin antibody clone B-5-1-2 ascites fluid 1:200 dilution (Sigma-Aldrich), secondary goat anti-mouse-Atto594 0.01 mg ml^{-1} (Atto-tec)	Leica TCS SP8 3X, 3-12% 570 nm illumination laser, 775 nm 0-403 mW STED laser, HyD: 600-640 nm, gain 200, pixel size 20 nm binned 2x, 8x line average, 200 Hz, gate 1-12 ns	Mowiol-DABCO
S14b,c,g,h	COS-7 microtubules-Atto490LS	COS-7 fixation and labeling, primary anti-tubulin antibody clone B-5-1-2 ascites fluid 1:100 dilution (Sigma-Aldrich), secondary donkey anti-mouse-biotin 1:200 dilution (Jackson ImmunoResearch), streptavidin-Atto490LS 0.01 mg ml^{-1} (Atto-tec)	Leica TCS SP8 3X, ~6.6-52.8 µW 495 nm illumination laser, 775 nm 0-403 mW STED laser, HyD: 645-720 nm, gain 200, pixel size 20 nm binned 2x, 8x line average, 200 Hz, gate 1-12 ns	Mowiol-DABCO
S14d	COS-7 microtubules-Abberior Star 635P	COS-7 fixation and labeling, primary anti-tubulin antibody clone B-5-1-2 ascites fluid 1:200 dilution (Sigma-Aldrich), secondary	Leica TCS SP8 3X, 11.2-89.6 µW 634 nm illumination laser, 775 nm 403 mW STED laser, HyD: 645-720 nm, gain 200,	Mowiol-DABCO

		goat anti-mouse-AbberiorStar635P 0.01 mg ml^{-1} (Abberior)	pixel size 20 nm binned 2x, 8x line average, 200 Hz	
S14e,f	COS-7 microtubules-Abberior Star 635P	COS-7 fixation and labeling, primary anti-tubulin antibody clone B-5-1-2 ascites fluid 1:200 dilution (Sigma-Aldrich), secondary goat anti-mouse-AbberiorStar635P 0.005 mg ml^{-1} (Abberior)	Leica TCS SP8 3X, 11.2 µW 635 nm illumination laser, 775 nm 0 mW STED laser, HyD: 645-720 nm, gain 200, pixel size 20-100 nm, 200 Hz, gate 0.3-12 ns	Mowiol-DABCO
S14g,h	COS-7 microtubules-Alexa594	COS-7 fixation and labeling, primary anti-tubulin antibody clone B-5-1-2 ascites fluid 1:200 dilution (Sigma-Aldrich), donkey anti-mouse-Alexa Fluor 594 antibody 0.005 mg ml^{-1} (Invitrogen)	Leica TCS SP8 3X, 4% 590 nm illumination laser, 775 nm 403 mW STED laser, HyD: 600-640 nm, gain 200, pixel size 20 nm binned 2x, 8x line average, 200 Hz, gate 1-12 ns	Mowiol-DABCO
S14g,i	COS-7 microtubules-Abberior Star 635P	COS-7 fixation and labeling, primary anti-tubulin antibody clone B-5-1-2 ascites fluid 1:200 dilution (Sigma-Aldrich), secondary goat anti-mouse-AbberiorStar635P 0.005 mg ml^{-1} (Abberior)	Leica TCS SP8 3X, 634 nm 179.2 µW illumination laser, 403 mW 775nm STED laser, HyD: 645-720nm, gain 100, pixel size 20 nm binned 2x, 8x average, 200 Hz, gate 0.8-11 ns	Mowiol-DABCO
S15	COS-7 microtubules-Abberior Star 635P same as 1	See above	Leica TCS SP8 3X, 11.2 µW 634 nm illumination laser, 201.5 mW 775 nm STED laser, HyD: 645-720 nm, gain 100, pixel size 15nm binned 2x	Mowiol-DABCO
S16	HeLa microtubules-Alexa647	HeLa fixation and labeling, primary anti-tubulin antibody clone DM1A 1:150 dilution (Abcam), donkey anti-mouse-Alexa Fluor 647 antibody 0.005 mg ml^{-1} (Invitrogen)	home-built widefield microscope, for details see materials & methods, excitation 635nm 1.9 kW cm^{-2}, 20 ms exposure time	50 mM MEA in 50 mM Tris-HCl pH 8.0 with oxygen scavenging, for details see materials & methods

12. *Bibliography*

1. Schmied, J. J. *et al.* Fluorescence and super-resolution standards based on DNA origami Flaws in evaluation schemes for pair- input computational predictions. *Nat. Methods* **9,** 1133–1134 (2012).

2. Szymborska, A. *et al.* Nuclear Pore Scaffold Structure Analyzed by Super-Resolution Microscopy and Particle Averaging. *Science* **341,** 655–659 (2013).

3. Bates, M. Single-particle analysis for fluorescence nanoscopy. *Nat. Methods* **15,** 3–4 (2018).

4. Descloux, A. *et al.* Combined multi-plane phase retrieval and super-resolution optical fluctuation imaging for 4D cell microscopy. *Nat. Photonics* **12,** 165–172 (2018).

5. Ovesny, M., Krizek, P., Borkovec, J., Svindrych, Z. & Hagen, G. M. ThunderSTORM : a comprehensive ImageJ plug-in for PALM and STORM data analysis and super-resolution imaging. *Bioinformatics* **30,** 2389–2390 (2014).

6. Mortensen, K. I., Churchman, L. S., Spudich, J. A. & Flyvbjerg, H. Optimized localization analysis for single-molecule tracking and super- resolution microscopy. *Nat Methods* **7,** (2010).

7. Huang, F. *et al.* Video-rate nanoscopy enabled by sCMOS camera-specific single-molecule localization algorithms. *Nat. Methods* **10,** 653–658 (2014).

8. Lambert, T. J. & Waters, J. C. Navigating challenges in the application of superresolution microscopy. *J. Cell Biol.* **216,** 53–63 (2016).

9. Nieuwenhuizen, R. P. J. *et al.* Measuring image resolution in optical nanoscopy. *Nat. Methods* **10,** 557–562 (2013).